arXiv:1204.1116v1 [astro-ph.EP] 5 Apr 2012

THE KILOMETER-SIZED MAIN BELT ASTEROID POPULATION REVEALED BY SPITZER

ERIN LEE RYAN[1], DONALD R. MIZUNO[2], SACHINDEV S. SHENOY[3], CHARLES E. WOODWARD[4], SEAN CAREY[5], ALBERTO NORIEGA-CRESPO[5], KATHLEEN E. KRAEMER[6], STEPHAN D. PRICE[6]

Received _____; accepted _____

AJ revised ver April 6, 2012

[1]Minnesota Institute for Astrophysics, University of Minnesota, 116 Church Street, S. E., Minneapolis, MN 55455, *erinleeryan@gmail.com*

[2]Institute for Scientific Research, Boston College, 140 Commonwealth Ave, Chestnut Hill, MA 02476-3862

[3]ORAU – NASA Ames Research Center, MS 245-6, Moffett Field, CA, 94035-0001

[4]Minnesota Institute for Astrophysics, University of Minnesota, 116 Church Street, S. E., Minneapolis, MN 55455

[5]Spitzer Science Center, MS 220-6, California Institute of Technology, Pasadena, CA 91125

[6]Institute for Scientific Research, Boston College, 855 Centre Street, Newton MA, 02459

ABSTRACT

Multi-epoch *Spitzer Space Telescope* 24 μm data is utilized from the MIPSGAL and Taurus Legacy surveys to detect asteroids based on their relative motion. These infrared detections are matched to known asteroids and rotationally averaged diameters and albedos are derived using the Near Earth Asteroid Model (NEATM) in conjunction with Monte Carlo simulations for 1835 asteroids ranging in size from 0.2 to 143.6 km. A small subsample of these objects was also detected by IRAS or MSX and the single wavelength albedo and diameter fits derived from this data are within 5% of the IRAS and/or MSX derived albedos and diameters demonstrating the robustness of our technique. The mean geometric albedo of the small main belt asteroids in this sample is $p_V = 0.138$ with a sample standard deviation of 0.105. The albedo distribution of this sample is far more diverse than the *IRAS* or *MSX* samples. The cumulative size-frequency distribution of asteroids in the main belt at small diameters is directly derived. Completeness limits of the optical and infrared surveys are discussed.

Subject headings: solar system: minor planets, asteroids: surveys

1. INTRODUCTION

Planetesimals are increasingly recognized as the evolutionary lynch pins for models of planet formation within the solar system. Their demographics, compositions, and dynamical attributes are imprints of our circumstellar ecosystem extant at the epoch of planet building that likely reflect the general conditions in exo-planetary disks. From the study of asteroids as relics of the early period of planet building, insight can be gained into the accretion processes and the initial composition of the proto-planetary disk.

Previous asteroid surveys performed with *IRAS* (Tedesco et al. 2002a) and *MSX* (Tedesco et al. 2002b) enabled estimates of the albedo and diameter distributions of large main belt asteroids (MBAs). These surveys were flux limited to an asteroid diameter threshold of $\gtrsim$10 km; however, they still produced albedo and diameter estimates for $\simeq$ 2000 asteroids. Recently, the NEOWISE survey Masiero et al. (2011) has released a preliminary catalog of albedos and diameters for $\simeq 10^6$ MBAs. This ensemble provided critical observational constraints for collisional models used to follow the evolution of planetesimals over the lifetime of the solar system (e.g., Bottke et al. 2005). These models use mean albedos for asteroids and their optical absolute magnitudes to generate the current day size-frequency distribution of asteroids. However, uncertainty exists regarding whether or not there is a tight and narrowly defined correlation between the albedos and diameters of asteroids. For instance, the *IRAS* survey suggests that the range of asteroid albedos becomes more diverse with decreasing diameter.

Compositional studies of main belt asteroids are utilized to explore whether or not our proto-planetary disk was contaminated by supernova products such as ^{26}Al. Early compositional studies (Gradie & Tedesco 1982) suggested evidence of a compositional gradient as a function of semi-major axis in the main belt - from highly thermally altered compositions in the inner belt to non-thermally altered compositions in the outer main

belt. This gradient was attributed to parent body melting due to heating by the decay of radioactive isotopes (Grimm & McSween 1993; McSween et al. 2002), and many models invoking this mechanism produced significant numbers of small thermally unaltered bodies in the inner main belt with diameters less than 20 km. However, this population has yet to be observed. For instance, the IRAS survey is incomplete for asteroids < 20 km at any zone in the main belt. Possibly, these small bodies were destroyed via mutual collisions (Davis et al. 1989), yet recent analysis of the Sloan Moving Object Catalog (SMOC; Carvano et al. 2010) indicates that many small ($\lesssim$10 km) dark asteroids were missed in prior asteroid surveys. In addition the SMOC data indicate that colors of small main belt asteroids display significant compositional diversity as a function of semi-major axis, rather than the zoning present in the large asteroid population.

The unique and unparalleled μJy point-source flux density sensitivity of the *Spitzer Space Telescope* during the cryogenic mission has enabled detection of faint asteroids with diameters as small as $\simeq$ 1 km at high signal to noise in both targeted surveys and serendipitous fields along the ecliptic. Here we utilize data from the MIPSGAL Galactic Plane survey and the Taurus Molecular Cloud survey to investigate the albedo behaviour of small asteroids, with a specific objective to determine whether or not the small ($\simeq$ 1 km) small main belt asteroids have the same mean albedo and spatial albedo distribution as the large ($\geq$ 10 km) main belt asteroids populations detected in earlier *IRAS* and *MSX* surveys. We use derived diameters from our MIPSGAL and Taurus catalogs to establish the size-frequency distribution of small main belt asteroids, and to assess whether the size-frequency distribution is functionally dependent on the heliocentric distance and/or composition.

In section 2, we briefly describe the mid-infrared (IR) surveys that were data-mined from the *Spitzer* archive to produce our asteroid catalog. Section 3 discusses our approach

to deriving asteroid albedos and diameters, while Section 4 discusses our thermal modeling results, survey completeness limits, comparisons to prior *IRAS* albedo catalogs of MBAs, as well as an examination of main belt albedo gradients, dynamical family albedos within the main belt and the overall bulk size-frequency distribution of asteroids. We conclude in Section 5.

2. MIPSGAL AND TAURUS SURVEYS

The two *Spitzer* surveys studied in this paper were selected via three criteria: multi-epoch 24 μm data taken with epoch separations on the scale of hours at ecliptic latitudes $\leq 20°$. More than 95% of all known main belt asteroids are found at inclinations $\leq 20°$, and studies have shown that the number counts of asteroids drop off by a factor of two from ecliptic latitudes of 0° to latitudes of 5° to 10° in the IR (Tedesco et al. 2005; Ryan et al. 2009). In order to detect the smallest, and thus faintest, asteroids in the *Spitzer* data, multiple epochs were required such that images from two epochs could be subtracted to remove fixed objects and allow for multiple detections of a single asteroid in an image pair. To properly derive diameters and albedos from thermal data, 24 μm fluxes are required as these fluxes are neither contaminated by reflected solar flux (as is the case for wavelengths shorter than ~ 5 μm, e.g., Ryan et al. 2009; Mueller et al. 2007), nor on the Wien side of the asteroid spectral energy distribution (SED) where thermal fitting errors are highest (Ryan & Woodward 2010; Harris et al. 2011). Two *Spitzer* surveys fulfilled these requirements – the MIPSGAL and the Taurus surveys.

The MIPSGAL survey (Carey et al. 2009, *Spitzer* Program ID 20597) was designed to survey 72 square degrees of the inner galactic plane at 24 and 70 μm with the Multiband Imaging Photometer for Spitzer (MIPS; Rieke et al. 2004). At low ecliptic latitudes (ecliptic latitudes from -1° to +14.2°), two epochs of MIPS Scan observations were taken with

separations of 3 to 7 hours to allow for asteroid rejection from the final image stacks over a total ecliptic survey area of 29.4 square degrees. The MIPSGAL data were obtained in Cycle-2 of the *Spitzer* cryogenic mission during the period 2005 September 27–29 UT.

The Taurus survey (Rebull et al. 2010, *Spitzer* Program ID Numbers 3584, 30816) was designed to survey approximately 30 square degrees in the Taurus Molecular Cloud at 24 and 70 μm with MIPS Scan observations. The Taurus Molecular Cloud is centered at $\sim 3^{\circ}$ ecliptic latitude, and all data of this region were taken at separate epochs at 5 to 12 hour intervals to allow for asteroid rejection from the final image stacks. This region was observed twice in two different years to obtain the required stacked survey depth; the total asteroid survey area is equal to 53.12 square degrees. The Taurus data were obtained in Cycle-1 and Cycle-3 of the *Spitzer* cryogenic mission during the periods 2005 February 27–March 2 UT and 2007 February 23–28 UT.

The MIPS 24 μm band imager is a 128×128 pixel Si:As impurity band conduction detector with an effective wavelength of 23.68 μm with a native pixel scale of $2\farcs49 \times 2\farcs60$. All 24 μm data are diffraction limited. All data obtained in the MIPSGAL and Taurus programs utilized the MIPS Scan Astronomical Observing Template with a Fast Scan Rate resulting in a total integration time per pixel of 15.7 secs in each AOR mosaic. The image data files selected for our analysis from MIPSGAL consists of 42 Astronomical Observing Requests (AORs) (21 pairs) reprocessed with the MIPSGAL processing pipeline of Mizuno et al. (2008), except that asteroids were not masked out of the AOR mosaics. The image data files selected for our analysis from the Taurus surveys consists of 30 AORs (15 pairs) processed by the data processing pipeline at the *Spitzer Science Center*. The pairs of images which shared a common image center were registered utilizing the world coordinate system (WCS) and differenced as illustrated in Figure 1. Image subtraction allows for removal of fixed point sources and galactic background structure. MOPEX

(Makovoz & Marleau 2005) was employed in conjunction with single epoch uncertainty maps to produce point-spread function (PSF) fitting photometry of the positive and negative sources in each difference image consisting of object positions, fluxes and 1-sigma uncertainties in the point source fitted fluxes.Positive and negative source catalogs were constrained to only report objects detected with PSF chi-squared normalized by the degrees of freedom in the PSF fit greater than one, which results in only returning objects detected at a signal-to-noise ratio of five (5) or greater.

Due to small world coordinate system offsets between epochs, some fixed sources are detected in both the positive and negative source catalogs. To fully remove these sources from the asteroid candidate catalogs, the positive and negative catalogs are cross matched. Any object with a partner in the opposite catalog with a position within a radius of 1.5 pixels is rejected from the asteroids candidate catalogs. Each candidate catalog is also searched for false sources present in the data due to increased sensitivity in small regions with increased areal coverage in an AOR which appear with predictable offsets given the scan rate. These latent sources were also removed from the final candidate catalogs.

Initial asteroid identification was performed utilizing known asteroids in the field. The JPL Horizons ISPY[1] tool was queried on 22 January 2011 to produce lists of all known asteroids present in the MIPSGAL and Taurus images and that time, the Horizons database contained the orbital elements for 543,357 known asteroids. The ISPY tool requires input of observation time and image corners and produces a list of known asteroids which would be present in the field, along with predicted positions, the predicted apparent magnitude, and the instantaneous rates of change in Right Ascension (RA.) and Declination (Decl.) at the time of observation in arcseconds per hour. The observation time given for all ISPY queries was the observation time of the first BCD image in the AOR mosaic. ISPY queries were

[1]http://ssc.spitzer.caltech.edu/warmmission/propkit/sso/horizons.pdf - Appendix 3

executed on an AOR basis, therefore for each subtracted image; two (2) ISPY queries were executed to predict the positions of the asteroids in each epoch. The predicted position at the start of an AOR, the AOR duration and the orbital rates are then convolved to define a search box for known asteroid candidates in each epoch. In 90% of cases, only one object from the candidate asteroid catalog is present in the search box. We interpret this coincidence as a direct object match. In the cases where multiple candidates are detected within a search box, the predicted position of the known object and the matched candidates are output to a file for visual inspection and recovery. A list of non-detected asteroids in each field is also produced to estimate the completeness of the 24 μm MIPS dataset.

All matched known asteroids and their corresponding predicted and detected positions, fluxes and orbital parameters are reported in Table 1. Columns in the flux table include asteroid name, Request Key of associated observation, date and time of observation, predicted RA. and Decl., detected RA. and Decl., a flux data flag, 24 μm flux and associated uncertainty, heliocentric distance (r_h) and *Spitzer*-to-asteroid distance, phase angle (α), and optical absolute magnitude (H). The flux flag has a value of 1 for all objects except in cases where asteroid flux varies by $\gtrsim$30% between two epochs, which is denoted with a flag of 2, or if an additional source such as a star is within $3\farcs75$, which is denoted with a flag of 3. Five hundred eighty-eight (588) known asteroids were detected only once in the *Spitzer* data, 1035 known asteroids were detected twice and 208 known asteroids were detected 3 or more times.

Eight (8) bright blended asteroid sources are present in the MIPSGAL and Taurus datasets. These asteroids are 103 Hera, 206 Hersilla, 2 33 Asterope, 318 Magdalena, 106 Dione, 1122 Neith, 283 Emma and 2007 McCuskey. Due to the extreme brightness of these sources these sources are "soft-saturated," and a single point source fitting result does not accurately measure the total flux from these objects. Fluxes for these objects were

recovered determining the relative flux ratio between the model 24 μm PSF central source and the first Airy ring and multiplying this ratio times asteroid fluxes in the first Airy ring. Positions in Table 1 are the nominal positions of the saturated PSF center and the uncertainty in the reported fluxes is assumed to be 15%. A flux flag value of 4 in Table 1 is used to denote the instances where the reported fluxes for these objects are reported from a saturated source.

Asteroid candidates with no association with known asteroids were not used for further diameter and albedo analysis. Estimating diameters and albedos for these objects is highly uncertain without the availability of optical absolute magnitudes, and derivation of orbits for these objects is problematic with only two epochs of data as acceleration vectors cannot be derived from the positional data.

3. ALBEDO DETERMINATION

We used the Near Earth Asteroid Thermal Model (NEATM; Harris 1998) to determine the rotationally averaged diameters and albedos of known asteroids in our MIPSGAL and Taurus samples. The NEATM relies upon a basic radiometric method to determine both the diameter and albedo of an asteroid (for a complete discussion, see Ryan & Woodward 2010). NEATM assumes balance between incident radiation and emitted radiation, where the emitted radiation has two components; a reflected and a thermal component. The reflected component has approximately same spectral energy distribution (SED) as the incident radiation; i.e., the reflected component is dominant in the optical and peaks in V band commensurate with the spectral region in which the sun emits the greatest flux. The reflected asteroid flux is proportional to the diameter of the body, $D(km)$ and the geometric albedo, p_V. To maintain energy balance the thermal flux is proportional to the amount of incident flux which is not reflected.

However, asteroids do not maintain one single body temperature, T(K), rather there is a temperature distribution across the surface which is then observed in the mid-IR. The NEATM utilizes an assumed temperature distribution to model the total IR flux, which is related to p_V. The temperature distribution utilized by NEATM is:

$$T_{NEATM}(\phi,\theta) = \left[\frac{(1-A)S_{\odot}}{\eta r_h^2 \epsilon \sigma}\right]^{\frac{1}{4}} (cos\phi)^{\frac{1}{4}} (cos\theta)^{\frac{1}{4}} \quad (1)$$

where the temperature, T is in Kelvin, A is the geometric Bond albedo, $S_{\odot}$ is the solar constant (W m^{-2}), r_h is the heliocentric distance (AU), ϵ is the emissivity of the object (assumed to be 0.9), σ is the Stefan-Boltzmann constant, η is the beaming parameter, ϕ is the latitude, and θ is longitude of the coordinate grid superposed on the asteroid. The derived temperatures are not phase angle dependent in the NEATM approach (Harris 1998).

In the NEATM temperature distribution, η, the beaming parameter is utilized as a variable to characterize both shape and thermal inertia. In an ideal case where an asteroid is a perfect sphere with zero thermal inertia, η equals unity. Only one thermal photometric measurement is available from the 24 μm measurements; therefore, NEATM was run with a fixed beaming parameter of $\eta = 1.07$. This value of η was selected by averaging the value of η for 1584 main belt, Hilda and Trojan asteroids observed by IRAS and/or MSX (i.e., Ryan & Woodward 2010). In addition we adopt a value for the emissivity (ϵ) of 0.9, a value appropriate for rock (Morrison 1973), and a phase slope parameter (G) of 0.15 when computing the asteroid diameter and albedo. To compute the geometric albedo and thus the temperature distribution on the illuminated face of the asteroid, one must anchor solutions to an optical data point. We utilized optical absolute magnitudes (H) from the

Minor Planet Center [2](MPC) for the purposes of our solutions.

The validity of our thermal models to compute rotationally averaged parameters of asteroids is robust and as yielded model albedo and diameters that are consistent with radar and occultation measurements of many tens of asteroids (e.g., Ryan & Woodward 2010).

All mean albedo and mean diameter solutions reported in Table 2 are derived from Monte Carlo modeling for each asteroid per sighting. A 500 data point distribution was created for each object observation such that the mean flux was equal to the flux measured by MOPEX and the standard deviation of the distribution was equivalent to the uncertainties in the flux measurement. These flux points were then used in conjunction the known orbital parameters and the H magnitude to produce albedo and diameter fitting results. In this Monte Carlo modelling, the optical absolute magnitude (H) was also varied by up to 0.2 magnitudes; equal to the mean offset in asteroid absolute magnitudes as derived from the MPC and the Asteroid Orbital Elements Database (ASTORB[3]; Bowell et al. 1989). Due to the wide width ($\Delta\lambda = 4.7$ μm) of the MIPS 24 μm channel, a color correction is also required to accurately fit the albedo and diameter. Our implementation of NEATM applies color corrections iteratively, such that a color correction is applied to the model asteroid flux with each refinement of the albedo (Ryan & Woodward 2010). Instead of using the subsolar temperature for the color correction, we calculate the mean of the temperature distribution for the application of the color correction, as described in Ryan & Woodward (2010). The standard deviation of the albedos and diameters listed in Table 2 are the 1-sigma statistical uncertainty ($\pm$) in the results added in quadrature with a $\pm$2% error in the absolute calibration of MIPS 24 μm data (Gordon et al. 2005). Results reported

[2]www.cfa.harvard.edu/iau/mpc.html

[3]ftp://ftp.lowell.edu/pub/elgb/astorb.html

in Table 2 are sorted by AOR Request Key and asteroid name/provisional designation allowing for direct matching of results with input data by line in Table 1. Table 3 is sorted in alphanumeric order and reports the mean albedo and diameter and associated 1-sigma uncertainties for 1831 asteroids, as well as the number of sightings used to arrive at these solutions.

4. THERMAL MODELLING RESULTS

4.1. Albedo and Diameter Properties/Validity

Prior observations and thermal model fits of the nine brightest sources, 103 Hera, 206 Hersilla, 233 Asterope, 318 Madgalena, 106 Dione, 1122 Neith, 283 Emma, 2007 McCuskey and 106 Aethusa derived using the NEATM and *IRAS* or *MSX* photometry were compared to those obtained from the MIPS photometry. Table 4 summarizes the albedos and diameters computed from the MIPS 24 μm data, and their *IRAS* or *MSX* derived NEATM albedo, diameter and beaming parameter (Ryan & Woodward 2010) and an occultation diameter if available from Dunham & Herald (2009). The diameter estimates from MIPSGAL photometry are within the uncertainties of those derived from fitting the SEDs produced by minimum of three wavelength specific fluxes from the *IRAS* and *MSX* surveys for all the objects. The thermal model solutions for the three asteroids with occultation derived diameters also match within 1%. This overlap in the diameter estimates suggests that the MIPSGAL and Taurus 24 μm solutions are robust, which is not surprising as we are observing thermal emission from asteroids at the peak of, or on the Rayleigh-Jeans tail of the SED. However, a slight variation in the mean diameters is present. This small spread in the distribution can be attributed to the use of a single mean beaming parameter of $\eta = 1.07$ for all asteroids in the MIPS data. This value of η must be used as there is insufficient photometry to allow for independent fits of albedo, diameter,

and beaming parameter simultaneously. Walker & Cohen (2002) in their analysis of *IRAS* Low Resolution Spectrometer (LRS) SEDs derive a mean $\eta = 0.98$ with a one sigma uncertainty of 0.08, commensurate with the value we adopt in our work. The agreement between *IRAS* and *Spitzer* results for these diameters is evidence that utilization of a single beaming parameter is appropriate for a bulk treatment of main belt asteroids.

Spitzer 70 μm data likely would provide an additional constraint on the derived characteristics of the sample asteroids. Unfortunately half of the 70 μm array malfunctioned, and the default MIPS scan AOT used for these observations leaves large gaps in the mosaics, resulting in a striped 70 μm mosaic wherein useful data only exists for half of the areal coverage of a 24 μm mosaic. This poor coverage coupled with the low sensitivity of 70 μm fast scan maps, which is insufficient to recover 90 km asteroids, led us to discard these data from our analysis.

Use of a single beaming parameter based on *IRAS* and *MSX* results assumes that small and large asteroid bodies have similar surface roughnesses and thermal inertia. For main belt asteroids with diameters > 20 km, thermal inertia and diameter are inversely proportional (Delbo & Tanga 2009) and this net effect would drive the beaming parameter to larger values. A similar effect of increasing thermal inertia with decreased size is noted within the Near Earth Asteroid population as well (Delbo et al. 2007). If a beaming parameter of 1.31 (equal to the mean from *IRAS* and *MSX* plus a 1-sigma standard deviation) is assumed for the 24 μm thermal modeling, the albedos differ from those reported here by $\leq 10\%$ and the albedos differ by $\sim 5\%$. If a beaming parameter of 0.77 (equal to the mean from *IRAS* and *MSX* minus a 1-sigma standard deviation) is used for the 24 μm thermal modelling, the albedos differ from those reported here by $\sim 30\%$ and the offsets are not systematic.

An additional source of albedo and diameter uncertainty is related to the reliability of

the optical absolute magnitudes provided by the MPC. A systematic color dependent offset was found between apparent V band magnitudes calculated using ASTORB (Bowell et al. 1989) orbital elements and absolute magnitudes and the synthetic V band photometry derived from the Sloan Digital Sky Survey (SDSS; Juric et al. 2002) of order 0.34 and 0.44 magnitude respectively for the blue and red populations of asteroids. This magnitude discrepancy is lessened to a 0.2 magnitude offset when MPC absolute magnitudes are used to derive a projected apparent magnitude. While a systematic offset in projected apparent magnitude could be the result of the SDSS using only two-body computations to calculate r_h, geocentric distance (Δ) and phase angle, the relative offset of 0.1 magnitudes between red and blue objects is accounted for in our Monte Carlo modelling allowance of $\pm$ 0.2 magnitude variation in the optical absolute magnitude H.

4.2. Completeness

To place the albedos and diameters in the MIPSGAL and Taurus catalogs in context, the effects of optical and IR completeness must be considered. To assess the completeness of optical asteroid surveys, we assume that they are complete to a V magnitude of 21.5, commensurate with the 95% completeness limit from the SDSS (Juric et al. 2002) and other surveys such as the Sub-Kilometer Asteroid Diameter Survey (Gladman et al. 2009) and Spacewatch (Larsen et al. 2007). Assuming that an asteroid will be detected at opposition by one of a number of surveys, we utilize the relation $m_V = H + 5log[r_h(r_h - 1)]$, and calculate the completeness limits in terms of H in each of the four main belt asteroids zones as defined in Zellner et al. (1975), adopting opposition and a heliocentric distance which corresponds to the outer semimajor axis range of each respective zone. These values range from absolute magnitudes of 18.6 in the inner main belt to 16.57 in the outer main belt. Unfortunately, many asteroid surveys are pencil beam surveys which do not cover the

full sky, therefore we estimate the full sky completeness of asteroid surveys utilizing the H magnitude distributions from the Minor Planet Center. We assume that all optical surveys are complete in each main belt region to the magnitude bin which contains the highest number of asteroid sources, and report those H magnitudes in Table 5. Values in Table 5 reflect both the completeness in terms of H and diameters assuming a mean asteroid geometric albedo $p_V = 0.02$ commensurate with the darkest observed asteroid albedos from any survey.

Queries of the Horizons database via the ISPY tool predict a total number of 7598 asteroid appearances for 3429 individual asteroids in the MIPSGAL and Taurus surveys. The catalog produced in this work contains 3486 sightings of 1831 individual asteroids, resulting in an overall object detection rate of $\sim 53\%$. There are three possible causes for this low recovery rate: rates of asteroid motion too low for the detection of movement between epochs; high rates of asteroid motion during a single AOR; and the mid-IR sensitivity completeness cut off. Those asteroids whose rates of motion would make them appear as fixed targets in the two epoch MIPSGAL data are Centaurs or Kuiper Belt objects. From the instantaneous rates of change in RA. and Decl. provided via the ISPY query, 32 objects are found to have rates of motion that would be insufficient for two epoch detection via the subtraction method for the shortest epoch separation of 3 hours. Near Earth asteroids (NEAs) are objects which move at such high rates that they may not be matched in an AOR due to smearing of the flux along the direction of motion. The rates of motion required for an asteroid source to move $1.2''$ (half of a native MIPS pixels) in an individual 5 sec BCD and a 15 sec stacked mosaic are ~ 1464 arcseconds per hour and ~ 293 arcseconds per hour, respectively. The asteroid 2002 AL14 has the greatest instantaneous predicted rate of motion of 186 arcseconds per hour in this survey data and was recovered in all three epochs where sightings were predicted. Therefore, the expected losses due to asteroid motion are biased towards non-detection of slowly moving objects in

both the MIPSGAL and Taurus datasets and the losses are less than 1% in total.

To assess the completeness of the 24 μm data, synthetic sources were added to single epoch MIPSGAL and Taurus AORs which were subsequently subtracted following the data analysis techniques described in Section 2. The 90% completeness limit was found to be 2 mJy for the MIPSGAL survey. We adopt this as the 24 μm completeness limit of both the MIPSGAL and Taurus surveys, although the Taurus survey is complete to 1.5 mJy due to a lack of extended background emission when compared to the MIPSGAL regions. At 24 μm, the fluxes of asteroids are most highly dependent upon diameter, not albedo. This enables completeness estimates as a function of diameter to be derived within the same zones utilized to analyze the optical completeness as reported in Table 5. These diameters were also calculated via the NEATM flux distribution with $\eta = 1.07$, assuming an object was observed at opposition (thus at a phase angle of zero degrees), and that the *Spitzer*-to-asteroid distance was 1 AU less than the heliocentric distance.

The asteroid completeness limits derived from the optical and the MIPSGAL and Taurus surveys are compatible; however, for all subsequent analysis, objects were removed which had fluxes less than the 24 μm completeness limit of 2 mJy or if they had an H magnitude greater than the optical completeness limit in their region. This constraint de-biases the *Spitzer* sample and resulted in the removal of 289 objects from the combined MIPSGAL and Taurus catalogs in the subsequent analysis; 280 for having H values less than the optical completeness, 4 for having fluxes less than the 24 μm completeness limit, and 5 for having both H values less than the optical completeness *and* fluxes less than the 24 μm completeness limit.

It is useful to compare the relative completeness of the MIPSGAL and Taurus surveys to the NEOWISE survey (Mainzer et al. 2011). With a mid-IR completeness limit of the NEOWISE survey currently unavailable (cf., Masiero et al. 2011), we utilize the H

magnitude distributions as a function of semi-major axis to compare relative completeness between the NEOWISE, MIPSGAL, and Taurus surveys. In the inner main belt, the H magnitudes of the NEOWISE survey peak at $H \simeq 15.5$ (Fig. 8 of Mainzer et al. 2011), whereas the mean H magnitude of the MIPSGAL and Taurus catalogs in the inner main belt is 15.8 mag as illustrated in Figure 2 once sources with H magnitudes greater than the optical completeness limit are removed. This offset of ~ 0.3 magnitudes between the NEOWISE and MIPSGAL and Taurus surveys is consistent in all semimajor axis zones. This offset translates roughly into a diameter difference of 0.5 km at any given albedo indicating that the *Spitzer* data is detecting asteroids at least 0.5 km *smaller* than NEOWISE survey at any given region of the asteroid belt.

This offset is confirmed also by a simple estimate of the asteroid diameters which can be detected by the WISE mission (Wright et al. 2010). Assuming a 5-σ limiting flux of 10 mJy at 22 μm, a beaming parameter, $\eta = 1.07$, geometric albedo $p_V = 0.14$, and an asteroid observed at opposition (phase angle $\alpha = 0$) at a heliocentric distance of 2.5 AU and a geocentric distance (Δ) of 1.5 AU, WISE can only detect asteroids with diameters $\gtrsim 1.65$ km, whereas under these s ame orbital assumptions and a flux completeness limit of 2 mJy, our *Spitzer* data is sensitive to asteroids with diameters $D \gtrsim 0.79$ km.

4.3. Albedo Catalog Comparision

The albedo distribution histogram from the MIPSGAL and Taurus surveys is presented in Figure 3. The albedo distribution derived for small asteroids is more diverse than the albedo distribution for large asteroids derived from *IRAS* and *MSX* data. The mean albedo for the complete *Spitzer* sample is 0.147 with a sample standard deviation of 0.104, whereas the mean albedo for the *IRAS* and *MSX* sample of 1584 objects in Ryan & Woodward (2010) is $p_V = 0.081$ with a sample standard deviation of 0.064. To test if these small and

large asteroid albedo distributions were selected from the same parent distribution, we performed a Komolgorov-Smirnov (K-S) test which rejected this hypothesis at the 99.99 percent level. We also performed a Wilcoxon-Mann-Whitney test to determine if these two albedo distributions were selected from a population with the same mean and that hypothesis was also rejected at the 99.99 percent level.

Studies of space weathering (Nesvorný et al. 2005; Clark et al. 2002, and references therein) indicate that young collisional fragments have different colors or higher albedos than old asteroids which have been subjected to solar wind exposure or micrometeorite impacts. Lunar space weathering causes microscopic melting of the surfaces and the formation of agglutinates. Impact melt causes submicroscopic metallic iron on the surfaces of lunar regolith particles (which in general are highly regular in shape, i.e., spherical) in cases where iron-bearing assemblages are extant on the surface (Keller et al. 1998, 1999; Pieters et al. 2000). The net effect is a reddened slope and decreased albedo with increasing exposure time. This lunar-type space weathering is assumed to modify the surfaces of asteroids as well, as minimal lunar-type space weathering is needed to match ordinary chondrite spectra to the spectra of S-type asteroids (Hapke 2000, 2001). However, analysis of asteroid regolith from the Hayabusa 25143 Itokawa sample return mission (Noguchi et al. 2011; Tsuchiyama et al. 2011) seems to suggest that asteroid the optical properties of asteroid surfaces may be altered by a combination of radiation-induced amorphization in addition to in situ reduction of regolith iron by solar wind irradiation. Whether or not the properties of the regolith dust from asteroid Itokawa are representative of all asteroids in general awaits further in situ sample return confirmation (Brucato et al. 2010; Lauretta et al. 2010).

Space weathering likely affects the albedo diversity we observe in our sample. Such diversity can be explained if lunar-type space weathering effects, comprising micrometeor

bombardment and solar wind irradiation, dominate. The distribution peak for carbonaceous asteroids is at a similar albedo for both large and small asteroids as there is insufficient iron bearing minerals for this iron sputtering on regolith particles. The high albedo tail of the small asteroid population also exhibits a greater diversity than the large asteroid population. A complication to this interpretation is that lunar-type space weathering has only been well studied with asteroids and mineralogies characteristic of the S- taxonomic type in observations and lab studies; the effects of solar wind exposure on compositions similar to C-type asteroids have not been the subject of laboratory investigation. Whether or not space weathering effects are germane is discussed further in Section 4.5, where characteristics of individual dynamical families within the main belt are compared.

4.4. Albedo gradient across Main Belt

A population of small thermally unaltered asteroids should exist in the inner main belt if ^{26}Al melting models are correct McSween et al. (2002); Grimm & McSween (1993). To critically examine this hypothesis, we have analyzed the albedo-orbital distribution of asteroids in the MIPSGAL and Taurus surveys, Figure 4, where the bulk albedo distribution of asteroids is color coded by albedo. The bulk albedo distribution, Figure 4 (*left*) can be contaminated by dynamical family members; for example a single family of many small S-type fragments can make the outer main belt appear silicate rich. To determine the effects of dynamical families on the heliocentric distribution of albedo types, our MIPSGAL and Taurus catalogs were cross referenced with the Dynamical Family Catalog of Nesvorný (2010) which utilized the proper elements for 293,368 asteroids to discriminate family memberships for 55 dynamical families. Of these 55 dynamical families, 47 are represented in our data and only eight families have more than 20 members in our combined MIPSGAL and Taurus albedo catalogs. Figure 4 (*right*) shows the resultant bulk albedo-orbital

distribution if these dynamical families are removed.

To compare the albedo distribution of small main belt asteroids in this dataset to those large asteroids detected by *IRAS* and *MSX*, we utilize the albedo definitions of S, X and C complex asteroids from Ryan & Woodward (2010) where C-types have $p_V \leq 0.08$, X-types are described by a geometric albedo $0.08 < p_V \leq 0.15$, and S-types span the range of geometric albedos $0.15 < p_V \leq 0.35$. The semimajor axis distribution of each classification from *IRAS* and MIPSGAL/Taurus is displayed in Figure 5. Though the semimajor axis distributions of S- and X-type asteroids appear similar between the *IRAS* and *Spitzer* surveys, the C-type distributions show a marked enhancement within the inner main belt. Removal of dynamical families, Figure 6, does not markedly change in the overall semimajor axis distribution of taxonomic type. Twenty-two percent (22%) of all small dark ($p_V \leq 0.08$) , presumably carbonaceous, asteroids reside in the inner main belt (2 AU $\leq$ a $\leq$ 2.5 AU). An enhancement of small C-type asteroids in the inner main belt is commensurate with the study of Carvano et al. (2010) who find that the distribution of small C- and X-type asteroids observed by the SDSS are fairly evenly distributed as a function of semimajor axis.

4.5. Dynamical family albedos

Of the 47 dynamical families represented in the *Spitzer* MIPSGAL and Taurus albedo catalog, eight Main Belt families have more than 20 family members when combined with the IRAS and MSX albedo catalog. When albedo and diameter are compared for each dynamical family, no trends of increasing albedo with decreasing diameter are seen within the Main Belt population (Figures 7 - 10) and the mean albedos of the families are consistent with the taxonomic type of their largest member, except in the case of the Nysa/Polana family (Table 6). The Nysa/Polana family (Figure 8) shows albedo evidence

for what may be two taxonomic types within the family – a very low albedo C-type asteroid grouping and a high albedo, S-type group. This split between the compositions of the family has been detected in the optical, where spectroscopic results found Nysa to be an S-type asteroid and Polana to be a C-type asteroid (Cellino et al. 2001). Although spectroscopically it was unclear if this subdivision in compositional types extended to small diameters, we find evidence of both taxonomic types amongst the small family members.

The lack of albedo trend with decreasing diameter within the main belt potentially vitiates the origin of the albedo offset between the *IRAS* and *Spitzer* datasets arising from space weathering due to solar wind implantation on asteroid surfaces. Although there is no direct way to measure asteroid age, a correlation between collisional timescale and asteroid diameter can be derived wherein the smaller asteroids are presumed to be on average younger than their larger neighbors (Davis et al. 2002). To explain the color offsets between ordinary chondrites and S-type asteroids, lunar-type space weathering from the solar wind irradiation has been preferred mechanism invoked (e.g., Sunshine et al. 2004; Nesvorný et al. 2005; Marchi et al. 2006) to account for the reddening of S-type asteroid slopes and a decrease in albedo with increasing asteroid age. The effects of space weathering are likely best understood by examining an asteroid population with a presumed common origin, such as the Koronis dynamical family, whose *Spitzer* derived albedos are presented in Figure 9, combined with the optical colors of asteroids within the Koronis dynamical family (Thomas et al. 2010), which indicate a trend towards a redder optical slope with increasing diameter. No trend towards an increased albedo is apparent in the 2 to 5 km diameter Koronis family population observed by *Spitzer*, although Thomas et al. (2010) argue that of a trend towards bluer colors exists in this size range. This trend, where the color reddens as a function of age but the geometric albedo shows little to no modification, is commensurate with the interpretation *Galileo* flyby data of Koronis family member, 243 Ida (Chapman 1996; Helfenstein et al. 1996). The *Galileo* imaging data of 243 Ida

shows large variations in spectroscopic absorption band depths and 1 and 2 μm related to $^{+2}$Fe; however, there is a lack of albedo variation commensurate with the varying surface color. Individual $\simeq$ 52 nm diameter, irregularly shaped dust particle samples returned from the surface of the S-type NEA Itokawa have amorphous rims populated by *small* nanophase iron particles with an average size of $\sim$ 2 nm (Noguchi et al. 2011). Laboratory measurements of small ($<$ 10 nm) nanophase iron particles indicate that these particles only redden reflectance spectra, and their presence in asteroid regolith would not result in a decreased albedo (Keller et al. 1999). To produce a reduction (darkening) of the albedo and a steeper slope to the reflectance spectra (reddening) requires vapor deposition of "larger" ($\lesssim$ 40 nm) metallic iron nanoparticles on grain rims (Noble et al. 2007; Pieters et al. 2000). The variation of spectroscopic band depths related to $^{+2}$Fe on 243 Ida without a related color variation could also be a signature derived from small nanophase iron particles deposited on the surfaces of individual regolith dust particles. In our *Spitzer* dataset, no trend is evident correlating an increasing albedo with decreasing diameter for the Koronis family and the other S-type families, including Flora, Eunomia and Eos. Hence, invoking traditional lunar-type space weathering mechanisms alone may not be sufficient to explain the relatively large albedo diversity within the small main belt asteroid population.

Our results wherein albedo does not change with diameter, and therefore age, coupled with results from *Galileo* and the *Hyabusa* mission suggests that the dominant space weathering mechanism is one which produces small nanophase iron particles. Lunar-type space weathering cannot be directly ruled out as the mechanism which causes space weathering within the asteroid belt. However as small nanophase iron particles do not modify the albedo, space weathering which produces these particles is insufficient to explain the relatively large fraction of small MBAs in the high albedo ($p_V > 0.15$) tail of the main belt asteroid albedo distribution. This observation suggests that the high albedo tail of the MBA albedo distribution is a function of composition, rather than space weathering.

4.6. Size-Frequency Distributions

From the MIPSGAL and Taurus data we can directly derive a size-frequency distribution (SFD) slope for small asteroids. Optical surveys such as the SDSS (Ivezić et al. 2001) and Spacewatch (Jedicke & Metcalfe 1998) have derived size-frequency distributions of main belt asteroids by assuming a mean albedo for all observed objects. The slope of the cumulative size frequency distributions, b, from the relation $N(> D) \propto D^{-b}$, as derived by these two surveys ranges from $b = 1.3$ to 1.8 respectively over an optical magnitude range $V \leq 21$. The cumulative SFD for all main belt asteroids in the *Spitzer* MIPSGAL and Taurus surveys is presented in Figure 11. The SFD between 7 and 25 km can be fit by a single power-law slope of b=2.34 ±0.05. The measured SFD deviates from this fitted slope by 3σ starting at 8 km. If one assumes that the break is a result of optical survey completeness, rather than a signature of the a transition between the regimes of asteroid strength dominated by material strength versus gravitational potential energy as predicted from laboratory studies (Holsapple 1994; Housen & Holsapple 1990), then it can be said that current optical asteroid surveys are only complete to $\sim$ 8 km. Removal of dynamical families from the *Spitzer* dataset modifies the power-law slope slightly; however, these changes in b are less than the derived uncertainties (±0.03).

A difference between power-law SFD slopes of asteroids was noted in the g′ and r′ filter surveys by Wiegert et al. (2007). Although it was unclear if this was an effect of color or albedo, the Wiegert et al. (2007) result can be tested with the MIPSGAL and Taurus data by using albedo as a proxy for composition. We have utilized the albedo ranges from Ryan & Woodward (2010) for S- and C-type taxonomic groups and present the SFDs in Figure 12. The slope of the C-type SFD between 8 and 25 km is $b = 2.49 \pm 0.07$, far shallower than the SFD slope of $b = 2.20 \pm 0.18$ derived for the S-type asteroids between 8 and 25 km in the MIPSGAL and Taurus catalogs. These *Spitzer* results are similar to the

slopes derived by Wiegert et al. (2007), indicating that difference between the SFD slopes derived in g′ and r′ filters were likely a function of composition/taxonomic type.

5. CONCLUSIONS

From the study of small Main Belt asteroids with *Spitzer*, we find that some these objects are more diverse than the large main belt asteroids observed by *IRAS* and *MSX*. The mean geometric albedo for small main belt asteroids is higher than that of large main belt asteroids and the overall range of albedo variation is greater for small asteroids by a factor of 2. The distribution of low albedo asteroids in the solar system is also very different for small and large asteroids; only 9% of all large (D $>$ 10 km) asteroids with C-type albedos are found in the inner Main Belt, but 24% of all small ($D < 10$ km) asteroids with C-type albedos are found in the inner main belt.

Though the extreme diversity of main belt asteroid albedos could be attributed to space weathering effects, this interpretation is not supported by the albedo results within dynamical families. Of the eight main belt dynamical families with more than 20 objects in the *Spitzer* and IRAS catalogs, none show the clear relationship of increasing albedo with decreasing diameter characteristic of lunar-type space weathering. To determine if this diverse albedo range is caused by space weathering or compositional variations optical colors and/or spectra of these small main belt asteroids will be required to discriminate compositional taxonomies.

The bulk size-frequency distribution (SFD) of the Main Belt utilizing asteroid diameters was derived directly from the *Spitzer* survey data. This bulk SFD shows evidence for a power-law break at 8.62 km. This asteroid diameter is consistent with the break diameter found for the Hilda group asteroid population (Ryan & Woodward 2010) and

suggests that asteroid diameters of $\simeq 8.5$ km lie at the transition boundary where smaller bodies are dominated by internal material strength, whereas larger bodies are bound by gravitational potential energy. This SFD break derived from measures of the small asteroid population (diameters down to ~ 1 km) occurs at larger diameters than those suggested from dynamical modeling of the evolution of these bodies (Bottke et al. 2005). Our *Spitzer* results therefore provide new observational constraint for collisional models that purport to follow the evolution of rocky planetesimals over the lifetime of the solar system.

ELR and CEW acknowledge support from National Science Foundation grant AST-0706980 to conduct this research. This work is based, in part, on archival data obtained with the *Spitzer Space Telescope*, which is operated by the Jet Propulsion Laboratory, California Institute of Technology under a contract with NASA. Support for this work was provided by an award issued by JPL/Caltech. The authors also wish to thank the meticulous reading of our manuscript by an anonymous referee whose insight helped to improve the narrative.

REFERENCES

Bottke, W. F., Durda, D. D., Nesvorný, D., Jedicke, R., Morbidelli, A., Vokrouhlický, D., & Levison, H. 2005, Icarus, 175, 111

Bowell, E., Hapke, B., Domingue, D., Lumme, K., Peltoniemi, J., & Harris, A. W. 1989, in Asteroids II, ed. R. P. Binzel, T. Gehrels, & M. S. Matthews (Tucson: Univ. Arizona Press), 524

Brucato, J. R., et al. in 38th COSPAR Sci. Assemb., 38, 642B

Carvano, J. M., Hasselmann, P. H., Lazzaro, D., & Mothé-Diniz, T. 2010, A&A, 510, A43

Carey, S.J., et al. 2009, PASP, 121, 76

Cellino, A., Zappalà, V., Doressoundiram, A., di Martino, M., Bendjoya, P. , Dotto, E., & Migliorini, F. 2001, Icarus, 152, 225

Chapman, C. 1996, Meteorit. Planet. Sci., 31, 699

Clark, B. E., Hapke, B., Pieters, C., & Britt, D. 2002 in Asteroids III, eds. Bottke Jr., W.F., Cellino, A., Paolicchi, P. & Binzel, R.P., (U. Arizona Press: Tucson), p. 585

Davis, D. R., Durda, D. D., Marzari, F., Campo Bagatin, A., & Gil-Hutton, R. 2002 in Asteroids III, eds. Bottke Jr., W.F., Cellino, A., Paolicchi, P. & Binzel, R.P., (U. Arizona Press: Tucson), p. 545

Davis, D. R., Weidenschilling, S. J., Farinella, P., Paolicchi, P., & Binzel, R. P. 1989 in Asteroids II, eds. Binzel, R. P., Gehrels, T. & Matthews, M. S., (U. Arizona Press: Tucson), 805

Delbo, M., Dell'Oro, A., Harris, A. W., Mottola, S., Mueller, M. 2007, Icarus, 190, 236

Delbo, M. & Tanga, P. 2009, Planet. Space Sci., 57, 259

Dohnanyi, J. S. 1969, J. Geophys. Res., 74, 2531

Dunham, D. W., & Herald, D. 2009, Asteroid Occultations V7.0. EAR-A-3- RDR-OCCULTATIONS-V7.0. NASA Planetary Data System

Fernández, Y. R., Jewitt, D., & Ziffer, J. E. 2009, AJ, 138, 240

Gladman, B. J. et al. 2009, Icarus, 202, 104

Gordon, K. D. et al. 2005, PASP, 117, 503

Gradie, J., & Tedesco, E. 1982, Science, 216, 1405

Grimm, R. E. & McSween, H. Y. 1993, Science, 259, 653

Hapke, B. 2001, J. Geophys. Res., 106, 10039

Hapke, B. 2000, Lunar and Planetary Institute Science Conference Abstracts, 31, 1087

Harris, A. W. 1998, Icarus, 131, 291

Harris, A. W., et al., 2011, AJ, 141, 75

Helfenstein, P. et al. 1996, Icarus, 120, 48

Holsapple, K. R. 1994, Planet. Space Sci., 42, 1067

Housen, K. R. & Holsapple, K. A. 1990, Icarus, 84, 226

Ivezić, Ž. et al. 2001, AJ, 122, 2749

Jedicke, R. & Metcalfe, T. S. 1998, Icarus, 131, 245

Juric, M. et al. 2002, AJ, 124, 1776

Keller, L. P., Wentworth, S. J., McKay, D. S., Taylor, L. A., Pieters, C., & Morris, R. V. 1999, New Views of the Moon 2: Understanding the Moon Through the Integration of Diverse Datasets, 32

Keller, L. P., Wentworth, S. J., & McKay, D. S. 1998, New Views of the Moon: Integrated Remotely Sensed, Geophysical, and Sample Datasets, 44

Larsen, J. A. et al. 2007, AJ, 133, 1247

Lauretta, D. S. et al. 2010, Meteorit. Planet. Sci. Suppl. 73, 5153L

Mainzer, A. et al. 2011, ApJ, 731, 53

Makovoz, D. & Marleau, F. R. 2005, PASP, 117, 1113

Marchi, S., Paolicchi, P., Lazzarin, M., & Magrin, S., 2006, AJ, 131, 1138

Masiero, J. R. et al., 2011, arVix:1109.4096v1

McSween, Jr., H. Y., Ghosh, A., Grimm, R. E.,Wilson, L., & Young, E. D. 2002 in Asteroids III, eds. Bottke Jr., W.F., Cellino, A., Paolicchi, P. & and Binzel, R.P., (U. Arizona Press: Tucson), p. 559

Mizuno, D. R. et al., 2008, PASP, 120, 1028

Morrison, D., 1973, Icarus, 19, 1

Mueller, M., Harris, A. W., & Fitzsimmons, A. 2007, Icarus, 187, 611

Nesvorný, D. 2010 Nesvorny HCM Asteroid Families V1.0. EAR-A-VARGBDET-5-NESVORNYFAM-V1.0. NASA Planetary Data System

Nesvorný, D., Jedicke, R., Whiteley, R. J., & Ivezić, Ž. 2005, Icarus, 173, 132

Noble, S. K., Keller, L. K., & Pieters, C. M. 2007, Meteorit. Planet. Sci., 45, 2007 (2011)

Noguchi, T. et al. 2011, Science, 333, 1121

Pieters, C. M. et al. 2000, Meteorit. Planet. Sci., 35, 1101

Rebull, L. M., Padgett, D. L., McCabe, C.-E., et al. 2010, ApJS, 186, 259

Rieke, G.H. et al., 2004, ApJS, 154, 25

Ryan, E. L. & Woodward, C. E. 2011, AJ, 141, 186

Ryan, E. L., & Woodward, C. E. 2010, AJ, 140, 933

Ryan, E. L. et al. 2009, AJ, 137, 5134

Sunshine, J. M., Bus, S. J., McCoy, T. J., Burbine, T. H., Corrigan, C. M., & Binzel, R. P. 2004, Meteorit. Planet. Sci., 38, 1343

Tedesco, E. F., Noah, P. V., Noah, M. & Price, S. D. 2002, AJ, 123, 1056

Tedesco, E. F., Egan, M. P. & Price, S. D. 2002, AJ, 124, 583

Tedesco, E. F., Cellino, A. & Zappala, V. 2005, AJ, 129, 2869

Tholen, D. J. 1989, Asteroids II, eds. Binzel, R. P., Gehrels, T. & Matthews, M. S., (U. Arizona Press: Tucson), 1139

Thomas, C. A., Rivkin, A. S, Trilling, D. E., Enga, M.-T., & Grier, J.A. 2010, Icarus, 212, 158

Tsuchiyama, A. et al. 2011, Science, 333, 1125

Walker, R. M., & Cohen, M. 2002, DPS 34.1416W

Wiegert, P., Balam, D., Moss, A., Veillet, C., Connors, M., & Shelton, I. 2007, AJ, 133, 1609

Wright, E. L. et al. 2010, AJ, 140, 1868

Zellner, B., Wisniewski, W. Z., Andersson, L., & Bowell, E. 1975, AJ, 80, 986

This manuscript was prepared with the AAS LaTeX macros v5.2.

Table 1. Orbital elements and 24 μm fluxes for asteroids detected in the MIPSGAL and Taurus Surveys

Name or Provisional Designation	Request Number	Date (UT)	Time (UT)	Predicted RA (Deg)	Predicted Dec (Deg)	Detected RA (Deg)	Detected Dec (Deg)	Flux Flag	24 μm Flux (mJy)	Flux Uncertainty (mJy)	Heliocentric Distance (AU)	Geocentric Distance (AU)	Phase Angle (Deg)	Absolute Magnitude	Absolute Magnitude $\pm$
1998KQ42	15598848	2005-09-28	07:28:19.89	273.74063	-15.64690	273.75385	-15.65198	1	24.950	0.345	1.72	1.21	12.03	15.300	0.150
2000AF141	15598848	2005-09-28	07:28:19.89	273.74564	-17.95830	273.75189	-17.95803	1	10.390	0.337	2.17	1.73	16.66	15.100	0.150
1998QD70	15598848	2005-09-28	07:28:19.89	273.84332	-17.12060	273.84808	-17.12097	1	22.830	0.432	2.81	2.44	20.02	14.100	0.150
2001TT94	15598848	2005-09-28	07:28:19.89	273.79892	-15.39880	273.80466	-15.39959	1	11.340	0.315	2.87	2.50	22.72	15.000	0.150
2001TK102	15598848	2005-09-28	07:28:19.89	273.80942	-17.00150	273.81311	-17.00447	1	20.590	0.469	3.47	3.14	16.88	14.300	0.150
2006RG52	15598848	2005-09-28	07:28:19.89	273.74466	-18.40490	273.74939	-18.40561	1	5.754	0.338	2.67	2.29	22.16	16.900	0.150

Note. — In column 9, the flux flags are the following: 1= asteroid flux which matches within 30% of flux in subsequent epochs, 2= flux which varies >30% btwn epochs, 3= nearby bright source, 4=blended bright source. The full catalog is will be available as a machine-readable table.

Table 2. Sighting solutions for asteroids detected in the MIPSGAL and Taurus Surveys

Name or Provisional Designation	Request Number	Geometric Albedo	Geometric Albedo Error	Diameter (km)	Diameter Error (km)
1998KQ42	15598848	0.35	0.04	1.95	0.20
2000AF141	15598848	0.36	0.04	2.12	0.22
1998QD70	15598848	0.15	0.02	5.23	0.53
2001TT94	15598848	0.12	0.01	3.86	0.39
2001TK102	15598848	0.06	0.01	7.38	0.75
2006RG52	15598848	0.06	0.01	2.35	0.24

Note. — The full catalog is will be available as a machine-readable table.

Table 3. Mean asteroid geometric albedos and diameters

Name or Provisional Designation	Geometric Albedo	Geometric Albedo Error	Diameter (km)	Diameter Error (km)	Number Observations
1321T-2	0.20	0.05	1.71	0.34	2
1413T-2	0.04	0.01	1.74	0.26	1
1978VE10	0.08	0.01	8.39	1.26	1
1978VE6	0.14	0.04	2.96	0.52	2
1978VZ5	0.18	0.03	4.79	0.70	2
1979MM2	0.39	0.06	1.69	0.25	1
1980FY2	0.212	0.03	5.46	0.82	1
1981EA29	0.05	0.01	8.29	1.26	2

Note. — The full catalog is will be available as a machine-readable table.

Table 4. Comparison of Spitzer derived albedos and diameters to IRAS/MSX and Occultation Diameters

Asteroid Name	MIPS Geometric Albedo	MIPS Diameter (km)	IRAS/MSX Geometric Albedo	IRAS/MSX Diameter (km)	Occultation Diameter (km)
103 Hera	0.20 ± 0.04	88.30 ± 8.51	0.19 ± 0.02	91.58 ± 4.14	89.1 ± 1.1
106 Dione	0.07 ± 0.01	168.72 ± 8.89	0.07 ±0.01	169.92 ±7.86	176.7 ± 0.4
206 Hersilia	0.06 ± 0.02	97.99 ± 7.40	0.06 ± 0.01	101.72 ± 5.18	
233 Asterope	0.10 ± 0.01	97.54 ± 10.32	0.08 ± 0.01	109.56 ± 5.04	
283 Emma	0.03 ± 0.01	145.44 ± 7.72	0.03 ±0.01	145.70 ± 5.89	148.00 ±16.26
318 Magdalena	0.03 ± 0.01	105.32 ± 11.11	0.03 ± 0.01	106.08 ± 0.25	
1064 Aethusa	0.17 ±0.04	25.42 ±4.28	0.27 ±0.03	20.64 ±1.37	
1122 Neith	0.34 ± 0.02	13.81 ±0.73	0.34 ± 0.07	13.84 ± 1.46	
2007 McCuskey	0.03 ±0.01	35.26 ±3.74	0.07 ± 0.01	33.79 ±1.31	

Table 5. Completeness limits in the optical and 24 μm

Semimajor Axis Range (AU)	Optical Completeness H (mag)	Optical Completeness Diameter (km)	24 μm Completeness Diameter (km)
2.06 - 2.5	17.25	3.33	0.79
2.5 - 2.82	16.75	4.20	1.05
2.82- 3.27	16.25	5.28	1.47
3.27 - 3.65	15.75	6.65	1.88

Table 6. Geometric Albedos of Dynamical Families Derived from *Spitzer* Surveys

Dynamical Family	Heliocentric Distance (AU)	DeMeo Taxonomic Type	Tholen Taxonomic Type	Number of Members	Mean Geometric Albedo
Flora	2.20	Sw	S	47	0.207 ± 0.092
Vesta	2.36	V	V	42	0.272 ± 0.156
Nysa/Polana	2.42	S/B		68	0.146 ± 0.107
Eunomia	2.64	K	S	26	0.175 ± 0.101
Koronis	2.87	S	S	30	0.174 ± 0.051
Eos	3.01	K	S	78	0.128 ± 0.047
Themis	3.13	C	C	71	0.063 ± 0.035
Hygiea	3.14	C	C	40	0.071 ± 0.046

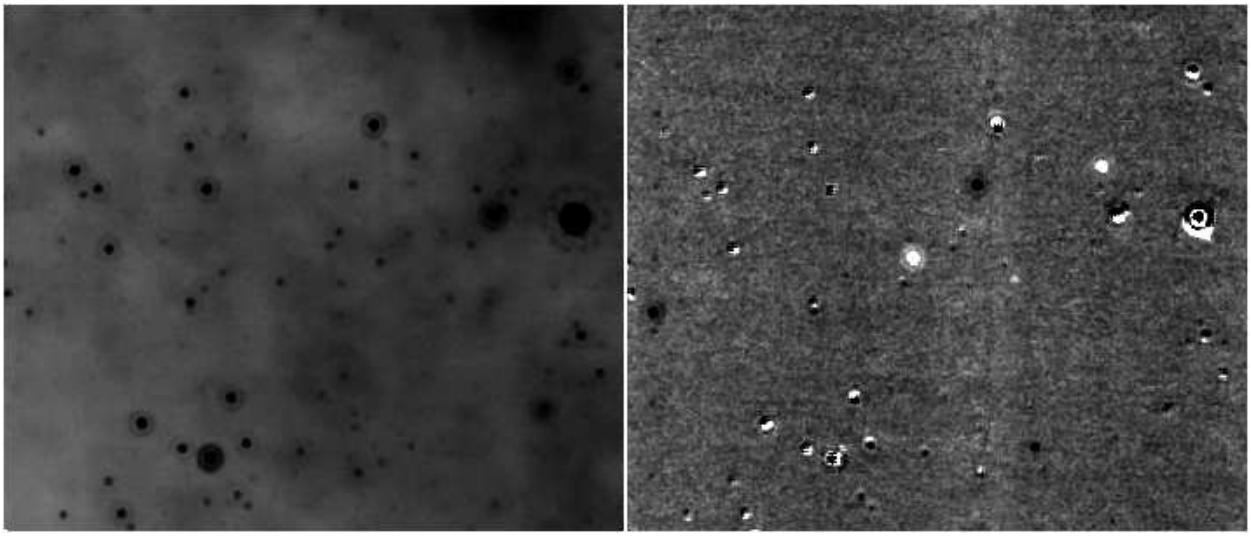

Fig. 1.— Epoch subtraction example from the MIPSGAL survey. Each image has a field of view of 8.75 × 6.96 arcminutes. On the left is a single AOR (Request Key 15619072) and on the right is the image that results from subtracting this image from its image pair, Request Key 15644416. The three asteroids seen in this frame are San Juan, Fienga and 1321 T-2.

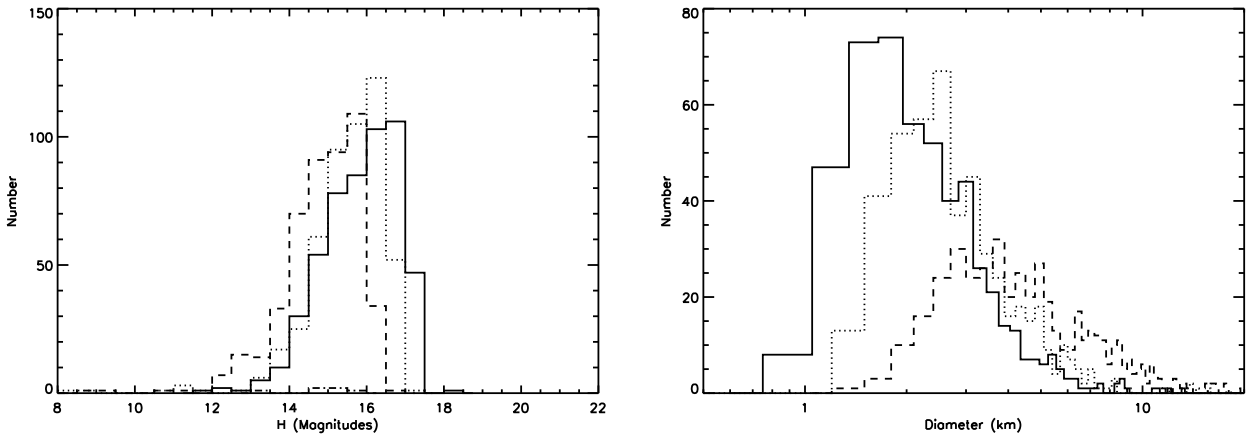

Fig. 2.— *Left:H* magnitude distributions of *Spitzer* detected asteroids: the solid line corresponds to the Zellner et al. (1975) Main Belt Asteroid (MBA) I region ($2.06 < a \leq 2.5$), the dotted line corresponds to MBAII ($2.5 < a \leq 2.82$), the dashed line corresponds to MBAIII ($2.82 < a \leq 3.27$). *Right:* Diameter distributions of the *Spitzer* detected asteroids in the same regions as the H magnitude distributions.

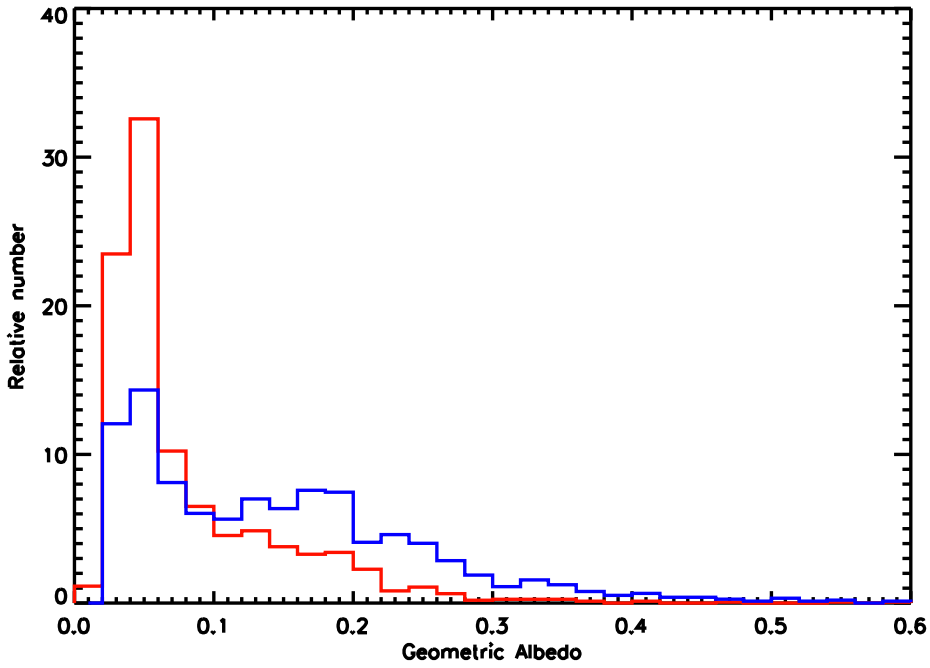

Fig. 3.— Albedo distribution for asteroids in the *IRAS* and *MSX* catalogs of Ryan & Woodward (2010) plotted in red and the albedo distribution for small Main Belt asteroids from the MIPSGAL and Taurus surveys shown in blue. The y-axis is percent of the total sample in each bin - addition of all y-values will equal 1 (100%)

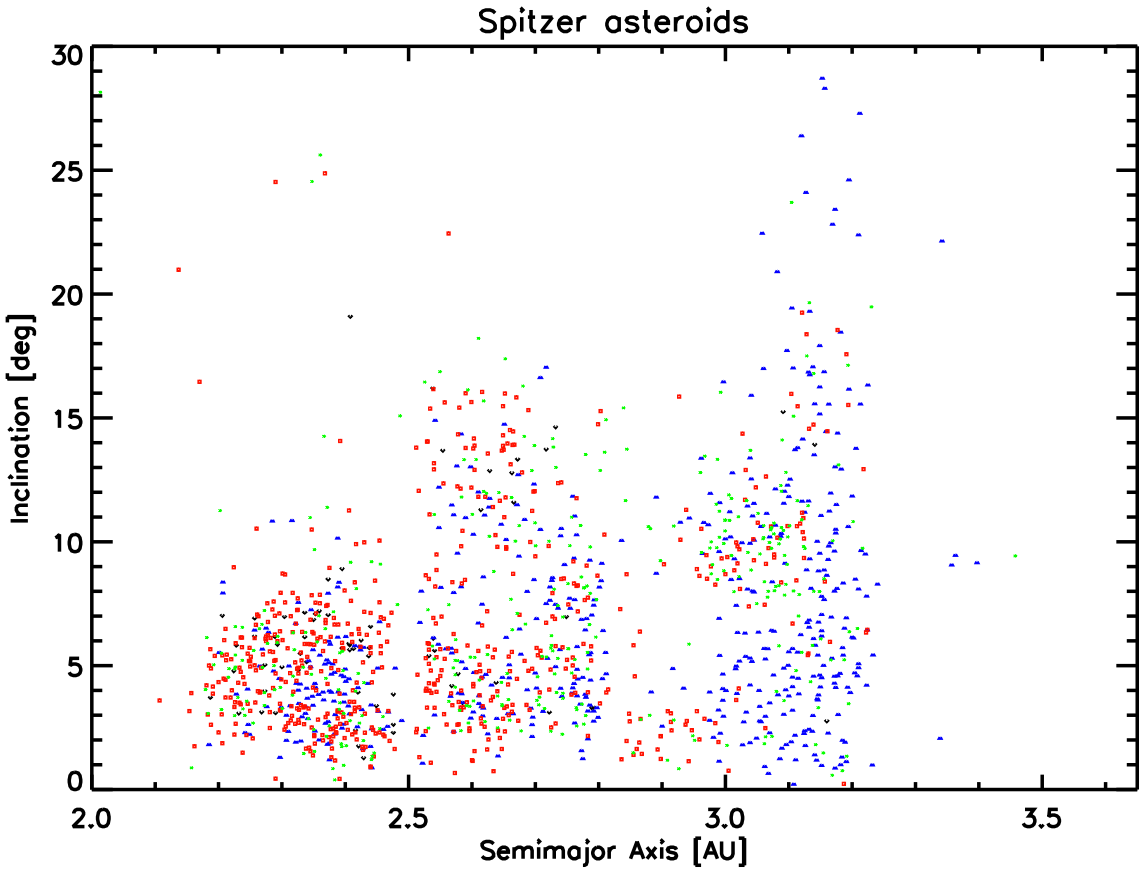

Fig. 4.— Orbital Element distribution of asteroids from the *Spitzer* MIPSGAL and Taurus surveys. Blue symbols correspond to asteroids with C-type albedos, green symbols correspond to asteroids with X-type albedos, and red symbols correspond to asteroids with S-type albedos. The panel includes all asteroids in the *Spitzer* catalogs.

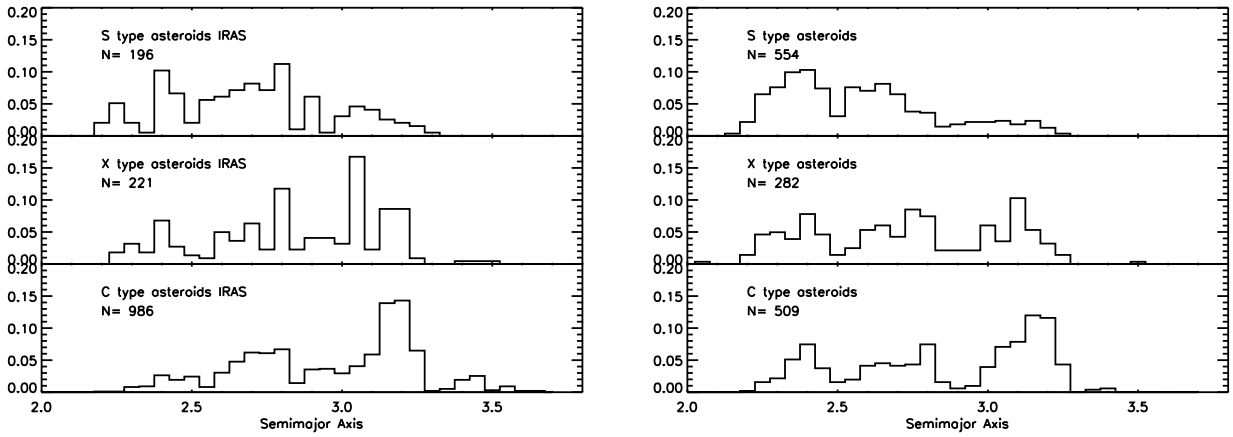

Fig. 5.— Heliocentric distance distribution of C-, X-, and S-type asteroids from the *IRAS* and *MSX* surveys (*left* panel) and this *Spitzer* work (*right* panel). The y-axis is the total percent of the taxonomic type in each bin of width 0.05 AU - addition of all y-values will equal 1.0

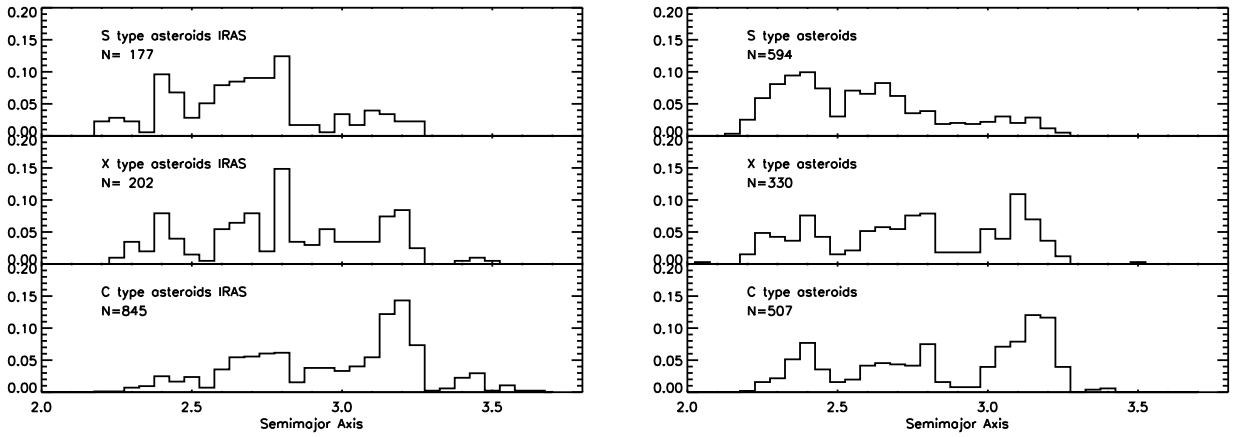

Fig. 6.— Heliocentric distance distribution of C-, X-, and S-type asteroids with all family members removed from the *IRAS* and *MSX* surveys (*left* panel, and *Spitzer* surveys on the *right*. The y-axis is the total percent of the taxonomic type in each bin of width 0.05 AU - addition of all y-values will equal 1.0

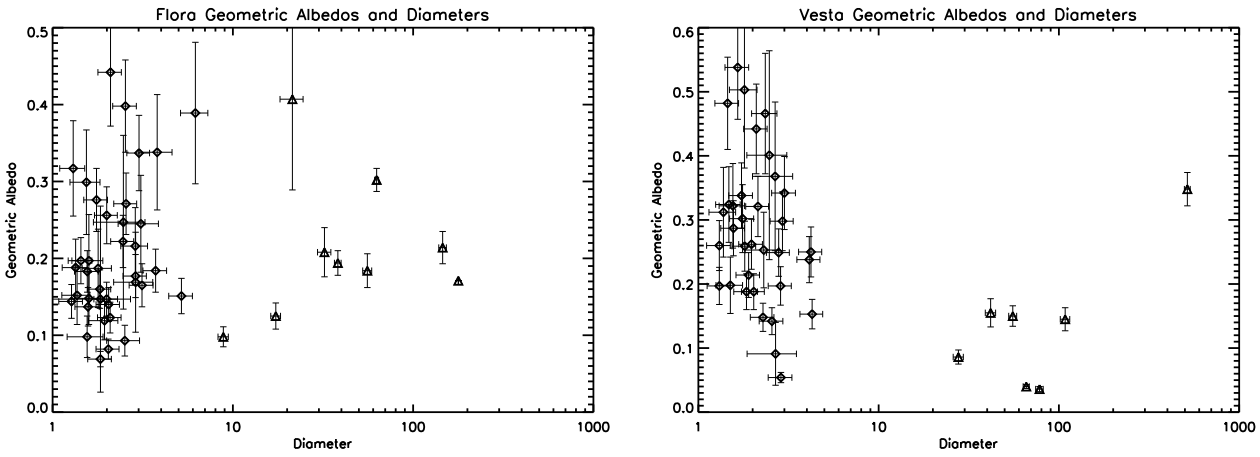

Fig. 7.— Left: Flora family albedo distribution as a function of diameter. Flora family asteroids with diameters > 10 km are from *IRAS*, those with diameters < 10 km are from *Spitzer*. Right: Vesta family albedo distribution as a function of diameter. Vesta family asteroids with diameters > 20 km are from *IRAS*, those with diameters < 20 km are from *Spitzer*.

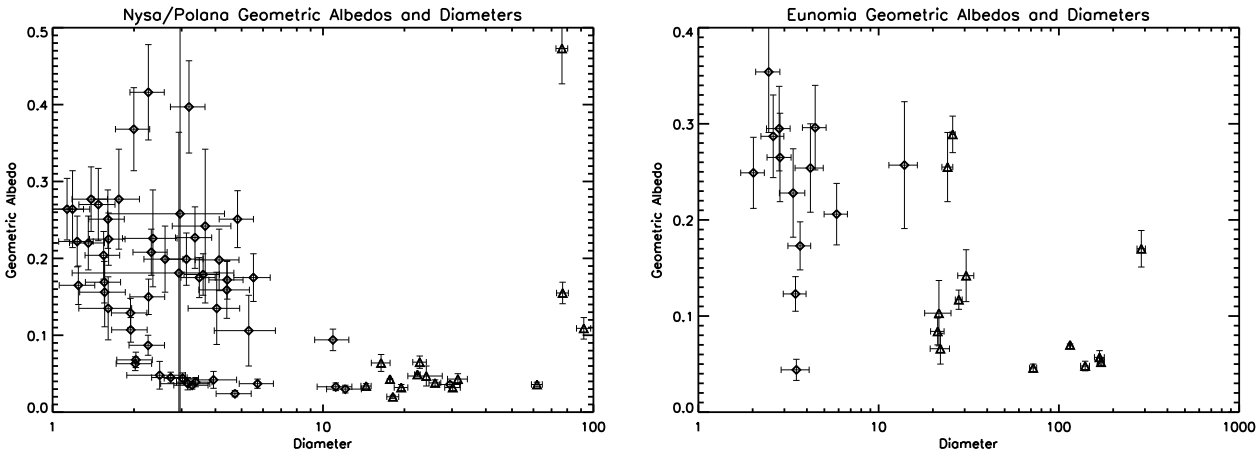

Fig. 8.— Left: Nysa/Polana family albedo distribution as a function of diameter. Nysa/Polana family asteroids with diameters > 10 km are from *IRAS*, those with diameters < 10 km are from *Spitzer*. Right: Eunomia family albedo distribution as a function of diameter. Eunomia family asteroids with diameters > 20 km are from *IRAS*, those with diameters < 20 km are from *Spitzer*.

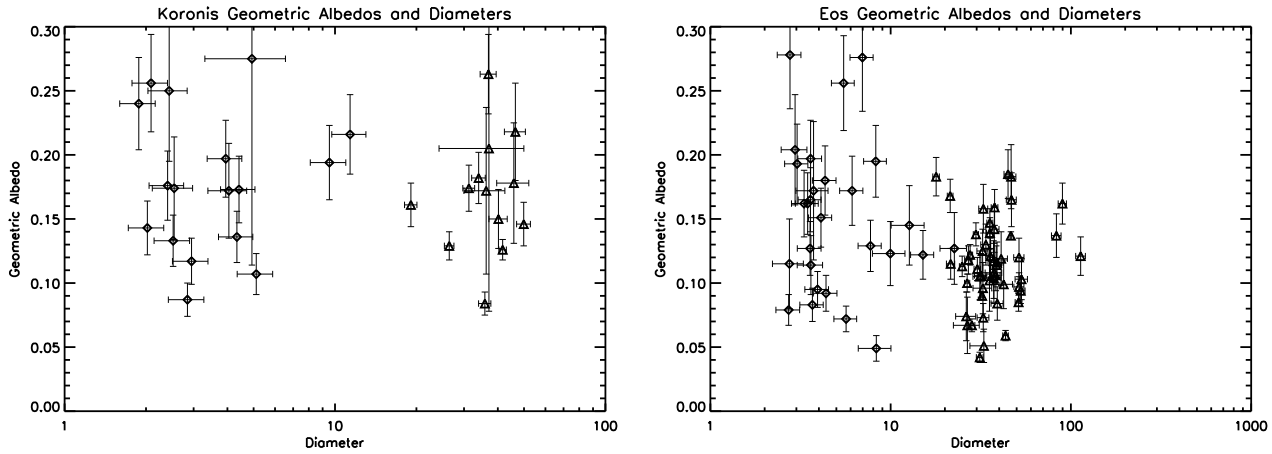

Fig. 9.— Left: Koronis family albedo distribution as a function of diameter. Koronis family asteroids with diameters > 20 km are from *IRAS*, those with diameters < 20 km are from *Spitzer*. Right: Eos family albedo distribution as a function of diameter. Eos family asteroids with diameters > 18 km are from *IRAS*, those with diameters < 18 km are from *Spitzer*.

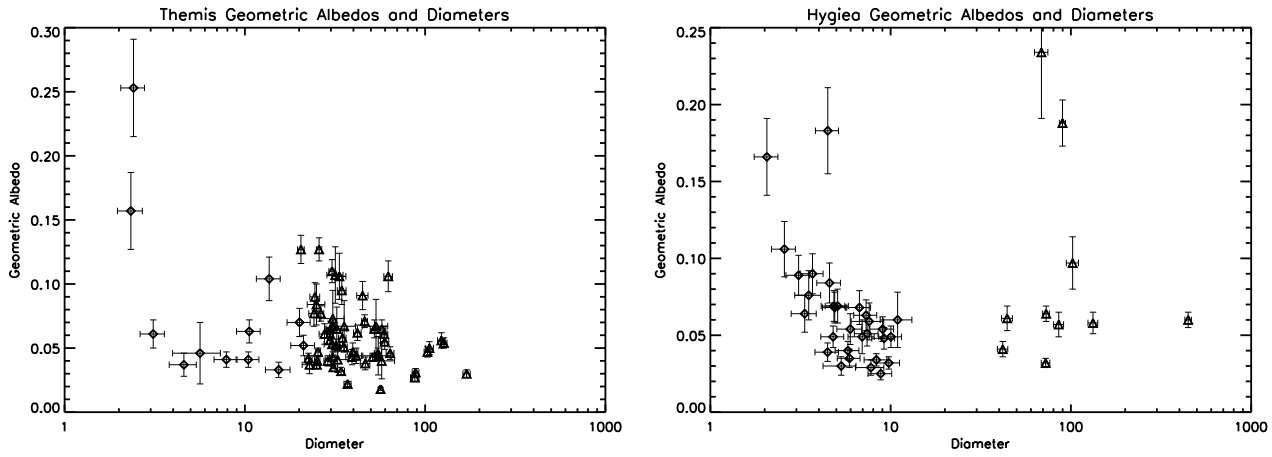

Fig. 10.— Left: Themis family albedo distribution as a function of diameter. Themis family asteroids with diameters > 20 km are from *IRAS*, those with diameters < 20 km are from *Spitzer*. Right: Hygiea family albedo distribution as a function of diameter. Hygiea family asteroids with diameters > 30 km are from *IRAS*, those with diameters < 10 km are from *Spitzer*.

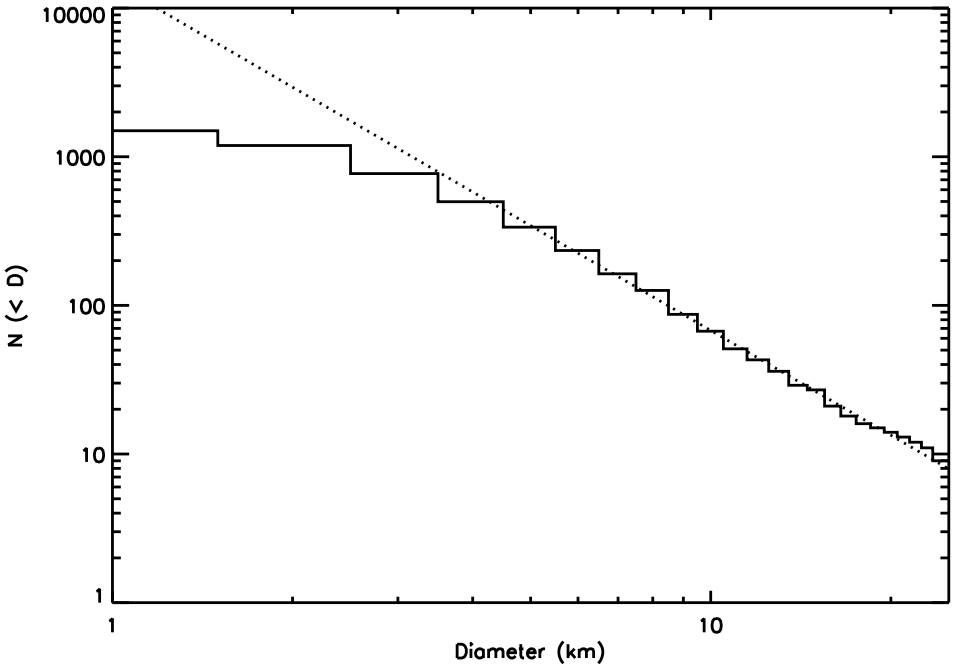

Fig. 11.— The cumulative size-frequency distribution (SFD) of the *Spitzer* catalogs is represented by the solid line. The dotted line represents the small diameter power-law fit where $b_1 = 2.02 \pm 0.06$, the dashed line represents the large diameter power-law fit where $b_2 = 3.04 \pm 0.05$.

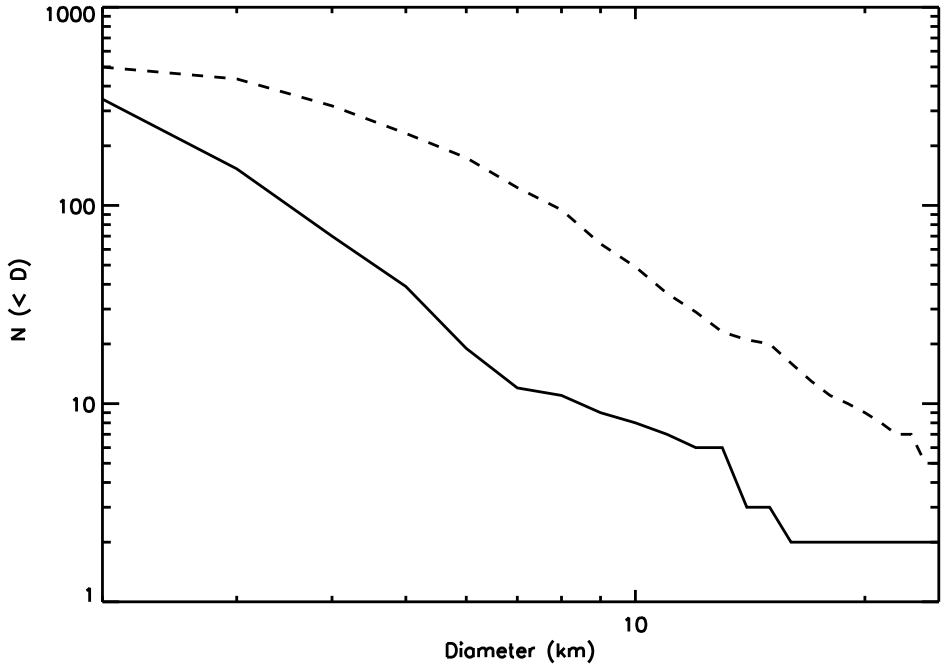

Fig. 12.— The cumulative size-frequency distribution (SFD) of S-type (solid line) and C-type (dashed line) asteroids from the *Spitzer* MIPSGAL and Taurus survey asteroid catalog.